CrossMark

J. Fluid Mech. (2021), *vol*. 923, R3, doi:10.1017/jfm.2021.597



Travelling waves in elliptic pipe flow

Ozge Ozcakir[1],† **and Philip Hall**[1]

[1]School of Mathematical Sciences, Monash University, Clayton, VIC 3800, Australia

(Received 7 April 2021; revised 22 May 2021; accepted 26 June 2021)

Families of exact coherent states in elliptical pipe flow obtained from the travelling-wave solutions in circular pipe flow by a continuation approach are found. Results are given in a regime of the aspect ratio A in which the laminar flow is linearly stable. The results suggest the possibility of two distinct classes of solutions of elliptical travelling waves at higher values of A: (i) rotationally symmetric centre-mode states that collapse towards the pipe centre and (ii) rotationally asymmetric vortex–wave interaction states with additional mirror symmetry exhibiting organization of the waves around a critical layer. These are the first calculations of three-dimensional travelling waves in elliptical pipes. Investigation of these states has the potential to provide fresh insight into the relationship between exact coherent structures in Poiseuille flow in pipes and channels.

Key words: nonlinear instability, transition to turbulence

1. Introduction

The flow in elliptical pipes is of considerable interest, not least because it bridges the gap between flows in a circular pipe and in a channel. If the ellipticity of the pipe is small, so that the cross-section is almost a circle, then the flow approximates Hagen–Poiseuille flow, which is generally believed to be stable to infinitesimal disturbances. On the other hand, when the ellipticity is large, so that the major axis of the ellipse is much longer than the minor axis, the laminar flow approximates plane Poiseuille flow and a critical Reynolds number exists. The linear stability problem in elliptical pipes was first considered for small ellipticity by Davey & Salwen (1994) and for large aspect ratio by Hocking (1977). Smith (1979) investigated the stability properties of the base flow asymptotically at large Reynolds number for various aspect ratios. Later, numerical investigations of the linearized equations at finite aspect ratio by Kerswell & Davey (1996) showed that above an aspect ratio of approximately 10.4 the flow becomes linearly unstable to the spanwise-modulated analogue of the Orr–Sommerfeld mode to which plane Poiseuille flow first loses stability.

† Email address for correspondence: ozge.ozcakir@monash.edu

© The Author(s), 2021. Published by Cambridge University Press

https://doi.org/10.1017/jfm.2021.597 Published online by Cambridge University Press

In the last few decades, there has been much interest in numerical investigation of three-dimensional exact coherent structures often referred to as travelling waves (TWs) in shear flows. It is believed that for moderate to large Reynolds number Re, these equilibrium solutions correspond to coherent states in a turbulent flow that are observable experimentally if the unstable manifolds of these states are sufficiently low-dimensional and their evolution in time is slow. Thus for example Hof *et al.* (2004) found experimentally in pipe flow that the flow migrates between different TW states. Smith & Bodonyi (1982) were the first to calculate such states and found that finite-amplitude helical waves were possible at large Re; these were later verified numerically by Deguchi & Walton (2013).

The physical mechanism to sustain such steady states for large Re is now well understood; it is the vortex–wave interaction scenario discussed by Hall & Smith (1991), henceforth referred to as VWI. In VWI, small-amplitude linear waves drive the rolls which themselves drive the streak through Reynolds stresses where the wave amplitude is largest in a critical layer. Note that the VWI formulation applies to unidirectional shear flows in channels or pipes of arbitrary cross-section (Deguchi & Hall 2014).

For pipe flow, various TWs have been calculated numerically with different degrees of rotational symmetry at finite and small Re (see e.g. Faisst & Eckhardt 2003; Wedin & Kerswell 2004; Viswanath 2009). Later, Ozcakir *et al.* (2016) investigated these states using numerical and asymptotic techniques and reported connections between a class of solutions computed by Wedin & Kerswell (2004) and the VWI asymptotic theory of Hall & Smith (1991). In addition to the VWI states based on the Hall & Smith (1991) asymptotics, Ozcakir *et al.* (2016) also gave an asymptotic structure of modes concentrated near the centre of the pipe, which they called nonlinear viscous core (NVC) states. These are 'centre modes' generated in a fully nonlinear viscous region of size $O(R^{-1/4})$ at the centre of the pipe. Unlike the VWI states, in this asymptotic case, there is no meaningful separation in scales between rolls, streaks and waves, and the interaction between different axial wavenumber components is fully nonlinear as $Re \to \infty$. From the agreement of the phase speed c versus the Reynolds number Re relation over a certain range of Re for a particular axial wavenumber, it appears that the so-called M- and N-class solutions of Pringle & Kerswell (2007) with twofold azimuthal symmetry are finite-Re realizations of VWI and NVC states, respectively. It is likely that other computed TW solutions could also be classified in a similar manner based on their high-Re behaviour.

For plane Poiseuille flow, the first known families of TW solutions were obtained by homotopy continuation from plane Couette flow by Waleffe (2001), Waleffe (2003), Nagata & Deguchi (2013) and Gibson & Brand (2014). Subsequently, Park & Graham (2015) computed new families of TWs, which were classified as 'critical layer modes' if the flow dynamics was localized around the critical layer, or 'core modes' if the solutions were largest near the channel centre.

There have also been several studies in square duct flows; for example, see Wedin, Bottaro & Nagata (2009), which investigated TWs at finite Reynolds number numerically, and found similarities between these solutions and circular pipe flow despite their geometric differences. Okino (2011) extended these to rectangular ducts using homotopy and identified localized TWs somewhat similar to some solutions found here as the duct became wider.

The objective of this study is to seek three-dimensional exact solutions in elliptical pipe flow and investigate how centre and VWI modes are affected by the deformation of a circular pipe cross-section into an elliptical one. For the first time in the literature, we

https://doi.org/10.1017/jfm.2021.597 Published online by Cambridge University Press

compute TWs for pipes with elliptical cross-sections by a homotopy continuation. We do not attempt to determine all possible TW states numerically; we focus on the main features to shed some light on potential connections between TWs in pipe flow and plane Poiseuille flow. In § 2 we formulate the numerical problem in elliptical pipe. In § 3, we briefly describe some TW states and discuss their connection to TWs in circular pipes. Finally, we give some conclusions in § 4.

2. Problem description

In the present work, our concern is with an incompressible viscous fluid of kinematic viscosity ν in a pipe with elliptical cross-section $x^2/a^2 + y^2/b^2 = 1$ for various values of aspect ratio $A = a/b$. Following Kerswell & Davey (1996), the Reynolds number, Re, is based on the speed of the base flow at $x = y = 0$ and a length scale chosen as $\sqrt{(a^2 + b^2)/2}$, so that the semi-major and semi-minor axes of the pipe measure $\sqrt{1+\beta}$ and $\sqrt{1-\beta}$ respectively, with $\beta = (A^2 - 1)/(A^2 + 1)$ for given aspect ratio A. We describe the problem in a non-orthogonal elliptical coordinate system where a point (x, y) on the elliptical cross-section is defined by $x = \sqrt{1+\beta}\, r\cos\theta$ and $y = \sqrt{1-\beta}\, r\sin\theta$ for $0 < r \leq 1$ and $0 \leq \theta < 2\pi$.

We are looking for TW solutions of the Navier–Stokes equations for the perturbation velocity $\boldsymbol{v}(r, \theta, z - ct) = u\tilde{\boldsymbol{r}} + v\tilde{\boldsymbol{\theta}} + w\hat{\boldsymbol{z}}$ and pressure $p(r, \theta, z - ct)$, where

$$\tilde{\boldsymbol{r}} = \sqrt{1+\beta}\cos\theta\,\hat{\boldsymbol{x}} + \sqrt{1-\beta}\sin\theta\,\hat{\boldsymbol{y}}, \quad \tilde{\boldsymbol{\theta}} = -\sqrt{1+\beta}\sin\theta\,\hat{\boldsymbol{x}} + \sqrt{1-\beta}\cos\theta\,\hat{\boldsymbol{y}}, \tag{2.1a,b}$$

and $\hat{\boldsymbol{z}}$ is a unit vector in the axial direction. The pipe is aligned along the z-axis with the base flow $\boldsymbol{v}_B(r) = (1 - r^2)\hat{\boldsymbol{z}}$. We assume $\boldsymbol{v}(r, \theta, z - ct)$ and $p(r, \theta, z - ct)$ to be 2π-periodic in θ and $\alpha(z - ct)$, and we assume that $\boldsymbol{v}$ satisfies a no-slip boundary condition on the wall. The TWs discussed here correspond to a constant mean axial pressure gradient $-4Re^{-1}\hat{\boldsymbol{z}}$, which drives $\boldsymbol{v}_B$ in the unperturbed case.

The non-dimensional Navier–Stokes equations become

$$-c\boldsymbol{v} + \boldsymbol{v}\cdot\nabla\boldsymbol{v} + \boldsymbol{v}_B\cdot\nabla\boldsymbol{v} + \boldsymbol{v}\cdot\nabla\boldsymbol{v}_B = -\nabla p + \frac{1}{Re}\Delta\boldsymbol{v}, \quad \nabla\cdot\boldsymbol{v} = 0, \tag{2.2}$$

where

$$(\boldsymbol{v}\cdot\nabla)\boldsymbol{v} = \begin{pmatrix} u\dfrac{\partial u}{\partial r} + \dfrac{v}{r}\left(\dfrac{\partial u}{\partial\theta} - v\right) + w\dfrac{\partial u}{\partial z} \\ u\dfrac{\partial v}{\partial r} + \dfrac{v}{r}\left(\dfrac{\partial v}{\partial\theta} + u\right) + w\dfrac{\partial v}{\partial z} \\ u\dfrac{\partial w}{\partial r} + \dfrac{v}{r}\dfrac{\partial w}{\partial\theta} + w\dfrac{\partial w}{\partial z} \end{pmatrix}, \quad \nabla p = \begin{pmatrix} F_1(\theta)\dfrac{\partial p}{\partial r} + \dfrac{1}{r}F_3(\theta)\dfrac{\partial p}{\partial\theta} \\ F_3(\theta)\dfrac{\partial p}{\partial r} + \dfrac{1}{r}F_2(\theta)\dfrac{\partial p}{\partial\theta} \\ \dfrac{\partial p}{\partial z} \end{pmatrix} \tag{2.3a,b}$$

and

$$\Delta\boldsymbol{v} = \begin{pmatrix} \left(\Delta_e - \dfrac{1}{r^2}F_2(\theta)\right)u - \left(\dfrac{2}{r}F_3(\theta)\dfrac{\partial v}{\partial r} + \dfrac{2}{r^2}F_2(\theta)\dfrac{\partial v}{\partial\theta} - \dfrac{2}{r^2}F_3(\theta)v\right) \\ \left(\Delta_e - \dfrac{1}{r^2}F_2(\theta)\right)v + \left(\dfrac{2}{r}F_3(\theta)\dfrac{u}{\partial r} + 2\dfrac{1}{r^2}F_2(\theta)\dfrac{\partial u}{\partial\theta} - \dfrac{2}{r^2}F_3(\theta)u\right) \\ \Delta_e w \end{pmatrix}, \tag{2.4}$$

https://doi.org/10.1017/jfm.2021.597 Published online by Cambridge University Press

with

$$\Delta_e = F_1(\theta)\frac{\partial^2}{\partial r^2} + \frac{1}{r}F_2(\theta)\frac{\partial}{\partial r} + \frac{2}{r}F_3(\theta)\frac{\partial^2}{\partial r\partial\theta} + \frac{1}{r^2}F_2(\theta)\frac{\partial^2}{\partial\theta^2} - \frac{2}{r^2}F_3(\theta)\frac{\partial}{\partial\theta} + \frac{\partial^2}{\partial z^2} \tag{2.5}$$

and

$$F_1(\theta) = \frac{1-\beta\cos(2\theta)}{1-\beta^2}, \quad F_2(\theta) = \frac{1+\beta\cos(2\theta)}{1-\beta^2}, \quad F_3(\theta) = \frac{\beta\sin(2\theta)}{1-\beta^2}. \tag{2.6a–c}$$

The continuity equation takes the form

$$\frac{\partial u}{\partial r} + \frac{u}{r} + \frac{1}{r}\frac{\partial v}{\partial\theta} + \frac{\partial w}{\partial z} = 0. \tag{2.7}$$

This coordinate system reduces to cylindrical polar coordinates when $\beta = 0$, making it a convenient choice for numerical continuation methods. Solutions to (2.2) have been computed in Ozcakir *et al.* (2016) and others for a pipe with circular cross-section. Our procedure is to use these TWs for an initial guess in the Newton iteration procedure for TW solutions to determine TW states with higher aspect ratios. The TWs computed by Ozcakir *et al.* (2016) possess a number of important symmetries in a pipe of circular cross section and are defined as

$$(k_0\text{-fold rotation}) \quad \mathbb{R}_{k_0} : (u, v, w, p)(r, \theta, z) \to (u, v, w, p)(r, \theta + 2\pi/k_0, z), \tag{2.8a}$$

$$(\text{shift-and-reflect}) \quad \mathbb{S} : (u, v, w, p)(r, \theta, z) \to (u, -v, w, p)(r, -\theta, z + \pi/\alpha), \tag{2.8b}$$

$$(\text{shift-and-rotate}) \quad \Omega_{k_0} : (u, v, w, p)(r, \theta, z) \to (u, v, w, p)(r, \theta + \pi/k_0, z + \pi/\alpha), \tag{2.8c}$$

where k_0, α are the azimuthal and axial wavenumbers, respectively. For the flow in an elliptical pipe, we retain the $\mathbb{S}$ symmetry, i.e. the azimuthal phase is fixed. The $\mathbb{R}_{k_0}$ symmetry is relevant only for $k_0 = 1, 2$, because of the π-radian rotational symmetry of the ellipse. Also, the Ω_{k_0} symmetry is broken when $k_0 = 2$, because of terms proportional to $\cos 2\theta$ and $\sin 2\theta$ appearing in the equations of motion. Therefore, in our calculations we will only consider TWs with $\mathbb{S}$ symmetry in combination with $\mathbb{R}_1, \mathbb{R}_2$ and Ω_1 symmetries. It should be noted that when $k_0 = 1$, the Ω_1 symmetry together with $\mathbb{S}$ symmetry imply mirror symmetry about the $\theta = \pi/2$ plane, i.e. the y-axis on the xy-plane which corresponds to top–bottom symmetry when the pipe is rotated $\pi/2$ radians around its axis for $A < 1$.

Our computational method is based on a Galerkin truncation of the Fourier modes in θ and $\tilde{z} = z - ct$ and a Chebyshev representation in r which automatically accounts for the boundary condition; see Ozcakir *et al.* (2016) for details. We use the following truncated basis representation for the velocity $\boldsymbol{v} = (u, v, w)^T$, suitable for k_0-fold azimuthally

https://doi.org/10.1017/jfm.2021.597 Published online by Cambridge University Press

symmetric ($\mathbb{R}_{k_0}$) TWs with shift-and-reflect ($\mathbb{S}$) symmetry:

$$\boldsymbol{v} = \sum_{\substack{0\le j\le N\\ 0\le k\le M\\ 0\le l \text{ even}\le P}} \begin{pmatrix} (u^{(1)}_{jkl}\cos l\tilde{z} + u^{(2)}_{jkl}\sin l\tilde{z})\Phi_j(\hat{r};kk_0)\cos kk_0\theta \\ (v^{(1)}_{jkl}\cos l\tilde{z} + v^{(2)}_{jkl}\sin l\tilde{z})\Phi_j(\hat{r};kk_0)\sin kk_0\theta \\ (w^{(1)}_{jkl}\sin l\tilde{z} + w^{(2)}_{jkl}\cos l\tilde{z})\Psi_j(\hat{r};kk_0)\cos kk_0\theta \end{pmatrix}$$

$$+ \sum_{\substack{0\le j\le N\\ 0\le k\le M\\ 1\le l \text{ odd}\le P}} \begin{pmatrix} (u^{(1)}_{jkl}\cos l\tilde{z} + u^{(2)}_{jkl}\sin l\tilde{z})\Phi_j(\hat{r};kk_0)\sin kk_0\theta \\ (v^{(1)}_{jkl}\cos l\tilde{z} + v^{(2)}_{jkl}\sin l\tilde{z})\Phi_j(\hat{r};kk_0)\cos kk_0\theta \\ (w^{(1)}_{jkl}\sin l\tilde{z} + w^{(2)}_{jkl}\cos l\tilde{z})\Psi_j(\hat{r};kk_0)\sin kk_0\theta \end{pmatrix}, \tag{2.9}$$

where Φ_j, Ψ_j are appropriately chosen radial velocity functions satisfying no-slip boundary conditions and appropriate symmetry at the axis. Here N, M and P represent the truncation levels of the radial, azimuthal and axial basis elements, respectively. Using the truncated velocities in (2.9) for the perturbation velocity in (2.2) at a given set of collocation points in r results in a nonlinear algebraic system for $(\boldsymbol{X}, c)$ where $\boldsymbol{X} = \{u^{(i)}_{jkl}, v^{(i)}_{jkl}, w^{(i)}_{jkl}\}$. Newton's method is used to solve the resulting nonlinear set of equations using an efficient GMRES solver. The pressure is determined by the pressure Poisson equation.

3. Numerical results

In our simulations the non-dimensional parameters (Re, α) are defined in such a way that the x-intercept of the elliptical boundary is $\sqrt{1+\beta}$ and the y-intercept is $\sqrt{1-\beta}$. This non-dimensionalization does not allow us to compare flows at different aspect ratios, since both Re and α vary as the aspect ratio $\sqrt{1+\beta}/\sqrt{1-\beta}$ changes. Instead, we present our results using a non-dimensionalization with parameters $Re^* = \sqrt{1-\beta}Re$ and $\alpha^* = \sqrt{1-\beta}\,\alpha$, where the length scale is based on the y-axis. When $A > 1$ (or $\beta > 0$, equivalently), Re^* is also referred to as Re_{ppf}, the Reynolds number based on the minor axis, since it corresponds to the Reynolds number for the plane Poiseuille flow in the limit as the aspect ratio $A \to \infty$ (or $\beta \to 1$, equivalently). On the other hand, when $A < 1$, Re^* is based on the major-axis length scale, in which case the non-dimensional parameters based on the minor-axis length scale satisfy $Re_{ppf} = A\,Re^*$ and $\alpha_{ppf} = A\,\alpha^*$.

We first reproduce the linear stability of the base flow calculations of Kerswell & Davey (1996) at various aspect ratios $A > 1$. In figure 1, the least stable scaled eigenvalue $\mathrm{Re}(\alpha^* c)$ is shown as a function of $log_{10}(\alpha^*)$ at $Re^* = Re_{ppf} = 6000$. In our computational range, our calculations (shown by dashed blue curves) are indistinguishable from the grey curve, confirming excellent agreement with Kerswell & Davey (1996).

Next, we discuss our results for elliptical TWs with different rotational symmetries, computed using the continuation method, starting with lower-branch TWs for circular pipes. In the figures, different resolutions were used, ranging between $(N, M, P) = (85, 16, 5)$ and $(N, M, P) = (165, 72, 12)$. Significantly increasing each of N, M and P for particular Reynolds numbers in this range and comparing with baseline calculations showed that the calculation for the phase speed c was accurate to four significant digits, whereas that of the velocity was accurate to at least three digits for each velocity component u, v, w, using the infinity norm in the Fourier domain. A discussion of the

https://doi.org/10.1017/jfm.2021.597 Published online by Cambridge University Press

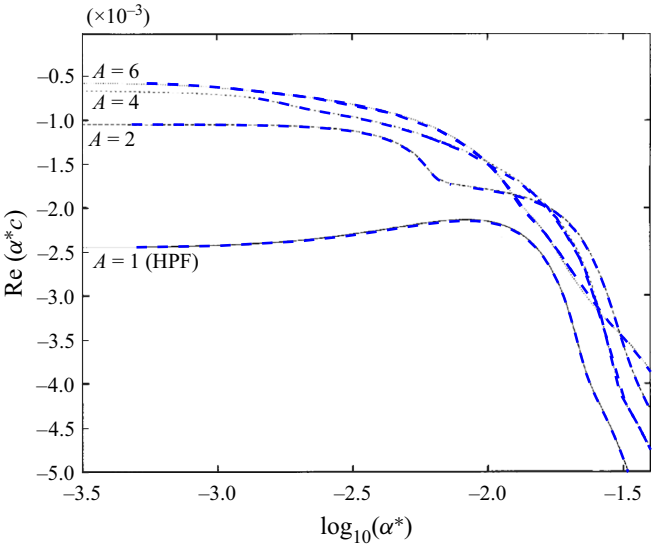


Figure 1. The least stable scaled eigenvalue $\mathrm{Re}(\alpha^* c)$ versus $\log_{10}(\alpha^*)$ for $Re^* = Re_{ppf} = 6000$ at various values of the aspect ratio A (blue dashed lines). For comparison the results of Kerswell & Davey (1996) are shown (grey lines).

resolution checks made can be found in the supplementary material available at https://doi.org/10.1017/jfm.2021.597.

Figure 2 displays c-versus-A continuation curves for rotationally symmetric ($k_0 = 2$) and rotationally asymmetric ($k_0 = 1$) TWs. The aspect ratio A was used as a homotopy parameter while keeping Re^* and α^* constant. Red curves indicate solutions with shift-and-reflect symmetry, while blue curves represent TWs with an additional shift-and-rotate symmetry. Coloured markers on the curves indicate TWs for circular pipes when $A = 1$ is used as the starting point of the continuation process. Again, it should be noted that $A > 1$ corresponds to $\beta > 0$, which means $Re_{ppf} = Re^*$ and $\alpha_{ppf} = \alpha^*$ remain constant as A varies. However, when $A < 1$, within the grey rectangular regions, Re_{ppf} and α_{ppf} will vary as A changes. Even though these results are not physically comparable to $A > 1$ solutions where Re_{ppf} is preserved, for $A < 1$ they are useful in generating new solutions, especially when $k_0 = 1$. In this case, the simple transformation $\boldsymbol{v}(r, \theta, z) \to \boldsymbol{v}(r, \theta + \pi/2, z)$ together with $A \to 1/A$ can be used to convert solutions for the aspect ratio $A < 1$ to solutions for the aspect ratio $1/A > 1$ for the same values of Re^* and α^*, with $Re_{ppf} = A\, Re^*$ and $\alpha_{ppf} = A\, \alpha^*$.

In figure 2(a), results for rotationally symmetric ($\mathbb{R}_2$) TWs at $Re^* = 7500$ and $\alpha^* = 1.55$ are shown. The blue, green, red and black markers at $A = 1$ respectively denote the C2, C1, WK2 and WK branches of solutions of Ozcakir, Hall & Tanveer (2019). The states C1 and C2 are centre modes, while WK and WK2 are VWI states. The WK2 and C2 branches possess shift-and-rotate Ω_2 symmetry in addition to the presumed shift-and-reflect $\mathbb{S}$ symmetry. Two continuation curves are generated, starting at a lower-branch WK solution, marked with a black dot, in the directions of increasing and decreasing aspect ratio A. Continuation curves cross the $A = 1$ vertical line multiple times, creating a figure of eight in a narrow regime with small ellipticity $0.7 < A < 1.4$. The two branches merge at a bifurcation point $A \approx 1.94$, and only one TW branch exists for high aspect ratios. Figure 2(b) shows rotationally asymmetric ($\mathbb{R}_1$) TWs at $Re^* = 5000$ and $\alpha^* = 1.437$.

https://doi.org/10.1017/jfm.2021.597 Published online by Cambridge University Press

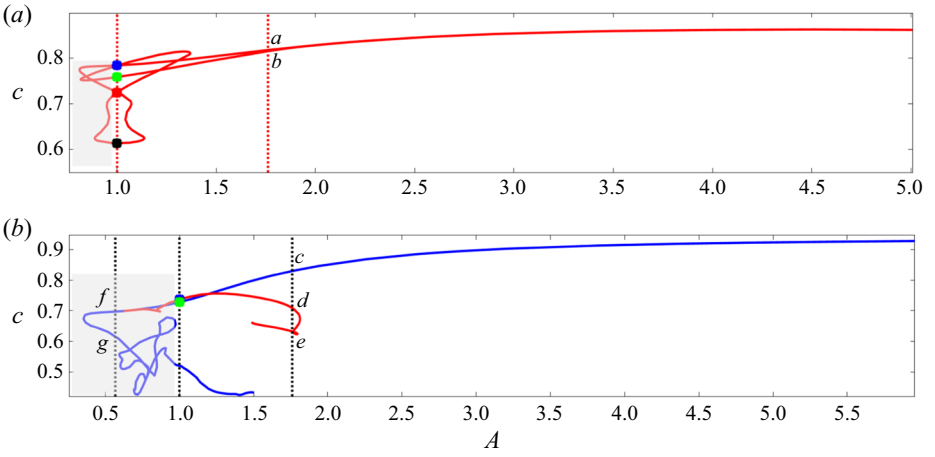


Figure 2. The wave speed c versus aspect ratio A for TWs with (a) rotational symmetry when $(Re^*, \alpha^*) = (7500, 1.55)$, and ($b$) rotational asymmetry when $(Re^*, \alpha^*) = (5000, 1.437)$. Vertical dotted lines correspond to $A = 1, A = 1.76$ and $A = 1/1.76$. Results for $A < 1$ are shown in grey rectangular boxes. The velocity fields at the points labelled a–f are shown in figure 3.

Coloured markers correspond to already known TW solutions of Pringle & Kerswell (2007) for circular pipes: S1 (blue dot), M1 (green dot) and N1 (red dot). These TWs, except S1, possess the additional shift-and-rotate symmetry Ω_1, which is essentially a mirror symmetry about $\theta = \pi/2$. In the regime of small ellipticity where $0.5 < A < 2$, multiple TWs exist, but as the ellipticity increases, only one branch survives, and it possess Ω_1 symmetry. This continuation curve is quite complex, becoming a somewhat tangled shape when $A < 1$, because the two parameters (Re_{ppf} and α_{ppf}) vary as A changes. One observation here is that the S1 solution is bifurcating from M1 at around $A \approx 0.7$ near the point labelled as (f), which shows that two distinct TWs in circular pipes are connected in the phase space when the geometry is perturbed slightly.

The perturbation velocity $\boldsymbol{v}$ can be written in the form $\boldsymbol{v} = \boldsymbol{U}(r, \theta) + \boldsymbol{v}_w(r, \theta, z - ct)$ with zero axial average over a period, denoted by $\langle \boldsymbol{v}_w \rangle = 0$. If we write $\boldsymbol{U}(r, \theta) = (U(r, \theta), V(r, \theta), W(r, \theta))$, then $(U(r, \theta), V(r, \theta), 0)$ is referred to as the roll part of the flow and represents streamwise vortices; $(0, 0, W(r, \theta))$ is termed the streak, while $\boldsymbol{v}_w(r, \theta, z - ct)$ represents the wave part of the flow. Figure 3 displays the cross-sectional velocity profiles for the streaks (left) and the waves (right) at the corresponding labelled points in figure 2. As described in the introduction, the structure and mechanism of TWs have been addressed by Hall & Sherwin (2010). Therefore, it is of interest to illustrate TWs found here in relation to the critical layer position. The black curves in the right-column contour plots show the position of the critical curve defined by $1 - r^2 + W(r, \theta) = c$. The axis of mirror symmetry is shown by a dashed line in figure 3(e–g). In all plots, the streaks remain the same size throughout the pipe, until wall effects become important. Figure 3(a,b) displays velocity fields corresponding to points labelled a and b in figure 2(a), with $k_0 = 2$, where the wave component of TWs are localized inside a core region and exhibit relatively strong deviations near the centre of the pipe. Figure 3(c–g) shows velocity fields that correspond to points labelled c–g in figure 2(b), for $k_0 = 1$, where the wave intensity is largest in a layer around the critical curve, as shown. Figure 3(f,g) with

https://doi.org/10.1017/jfm.2021.597 Published online by Cambridge University Press

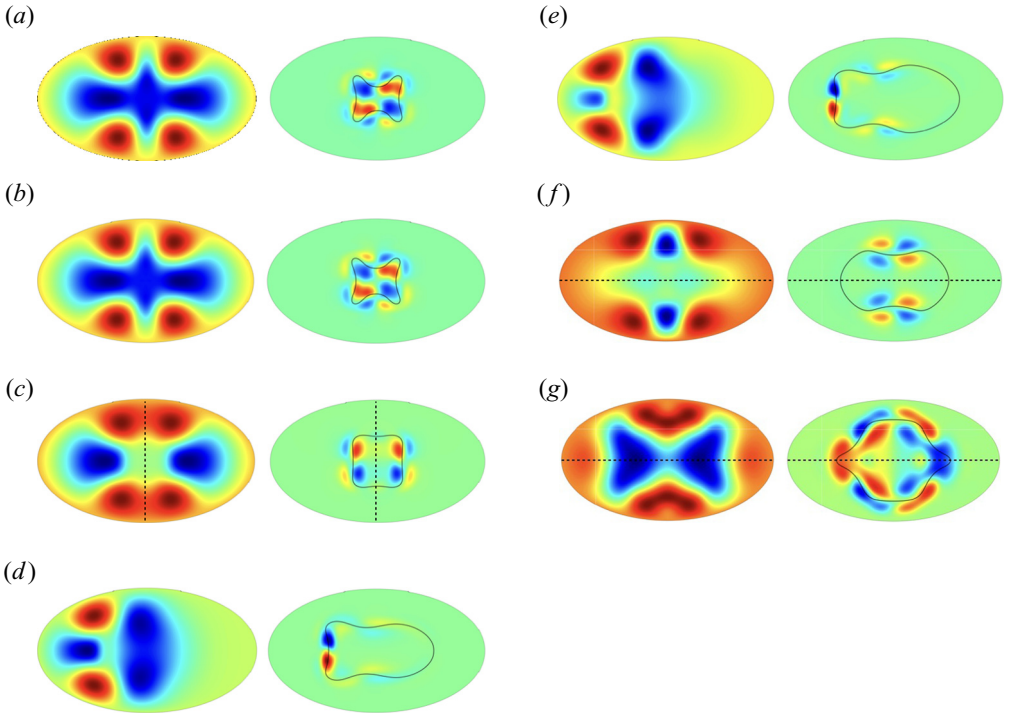


Figure 3. The cross-sectional velocity profiles for streaks (left) and waves (right) at corresponding points on figure 2 when $\tilde{z} = 0$ for $A = 1.76$ (a–e) and $A = 1/1.76$ (f,g). Contour colours range from dark red (largest positive) to dark blue (smallest negative). The black dashed lines in (e–g) show the axes of mirror symmetry. In (f,g), $Re_{ppf} = 2840.9$, and the results are displayed after a $\pi/2$-radian clockwise rotation around the origin.

$A = 1/1.76$ is particularly interesting, because these solutions give rise to TWs which possess top–bottom symmetry without its having been imposed numerically in the solver.

For large values of the aspect ratio A, new TW solutions are obtained by a continuation of the points labelled a and c in figure 2. The cross-sectional velocity profiles are shown in figures 4 and 5, respectively. In both figures 4(a) and 5(a), the streaks are becoming more localized around the pipe centre along the major axis; the critical layers stay close to the centre as A increases. In figure 4(b) the waves remain concentrated in a core region and appear to expand between just above the critical layer and the pipe centre, while in figure 5(b) the waves are largest around the critical layer. The clear organization of waves around the critical layer suggests suggests a connection to the critical layer dynamics of VWI.

Other classes of TWs can be obtained at high aspect ratios after careful investigation of the solutions in figure 2(b) by continuously increasing Re^* and decreasing the aspect ratio A. For example, starting at the point f, whose cross-section is shown in figure 3(f), we are able to compute a new TW at $A = 1/5.56$ to the desired accuracy as shown in figure 6. After a rotation by $\pi/2$ radians, this TW has top–bottom mirror symmetry with $A = 5.56$, and it has a wide, almost elliptical critical layer, with localized waves concentrated around the critical curve. Similar calculations can be done at the other labelled point g, but because of the computational cost, we did not attempt to do such calculations with high accuracy.

Figure 7 displays the wave speed c of TWs as a function of Re_{ppf} for $k_0 = 1$ (black) and $k_0 = 2$ (blue) solution branches for the aspect ratios $A = 1.76$ (solid), $A = 1/1.76$

https://doi.org/10.1017/jfm.2021.597 Published online by Cambridge University Press

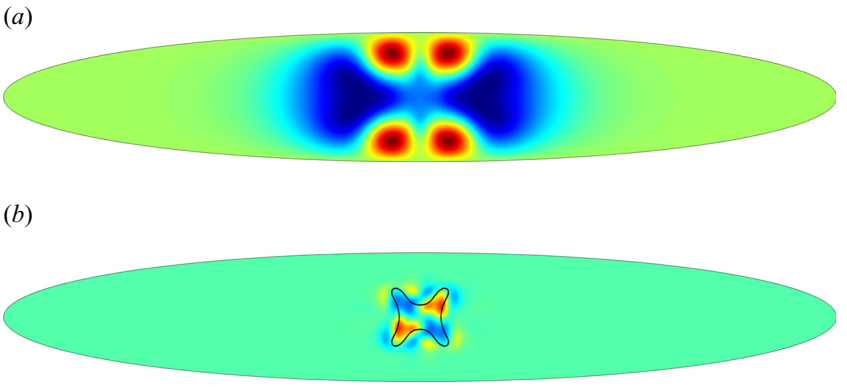


Figure 4. The cross-sectional plots of the perturbation velocity at $\tilde{z} = 0$ for streaks (a) and waves (b) for aspect ratio $A = 6.51$ when $(Re^*, \alpha^*) = (7500, 1.55)$ with $k_0 = 2$.

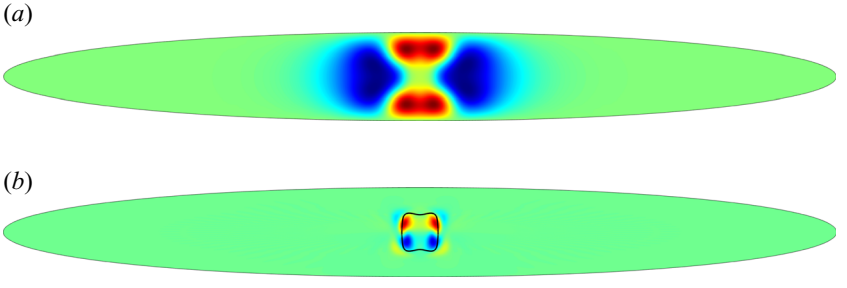


Figure 5. The cross-sectional plots of the perturbation velocity at $\tilde{z} = 0$ for streaks (a) and waves (b) for aspect ratio $A = 9.38$ when $(Re^*, \alpha^*) = (5000, 1.437)$ with $k_0 = 1$.

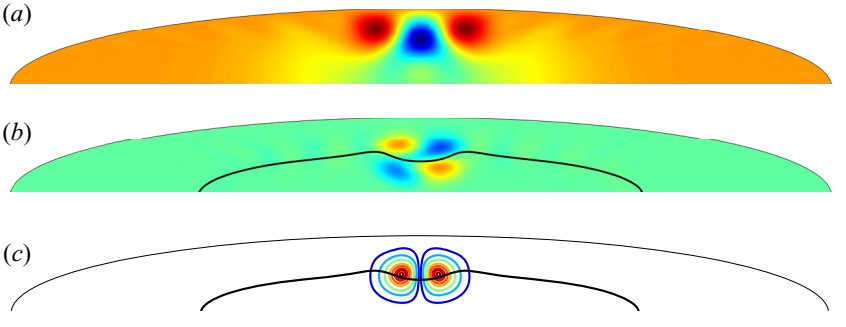


Figure 6. Cross-sectional plots of the perturbation velocity at $\tilde{z} = 0$ for streaks (a) and waves (b). (c) Contour lines of the magnitude of the fundamental Fourier harmonics $\|\boldsymbol{u}_1(r, \theta)\|$, where $\boldsymbol{u}(r, \theta, z) = \sum_{l=-P}^{P} \boldsymbol{u}_l(r, \theta) e^{i\alpha l z}$ when $A = 1/5.56$ and $(Re^*, \alpha^*) = (5000, 0.2719)$ with $k_0 = 1$ and $Re_{ppf} = 899.28$. Plots are rotated $\pi/2$ radians clockwise, and only the upper half of the pipe is shown, because of top–bottom mirror symmetry.

(dash-dotted), $A = 3.36$ (dashed) and $A = 9.38$ (dotted). The rotationally symmetric solutions ($k_0 = 2$) arise at much larger values of Re than the asymmetric solutions ($k_0 = 1$). The points labelled a–g in figure 2 are also marked as reference points, with the corresponding flow fields shown in figure 3. All of the TWs (except for $A = 9.38$) arise from saddle-node bifurcations. For each c-versus-Re_{ppf} curve, the two branches emanating

https://doi.org/10.1017/jfm.2021.597 Published online by Cambridge University Press

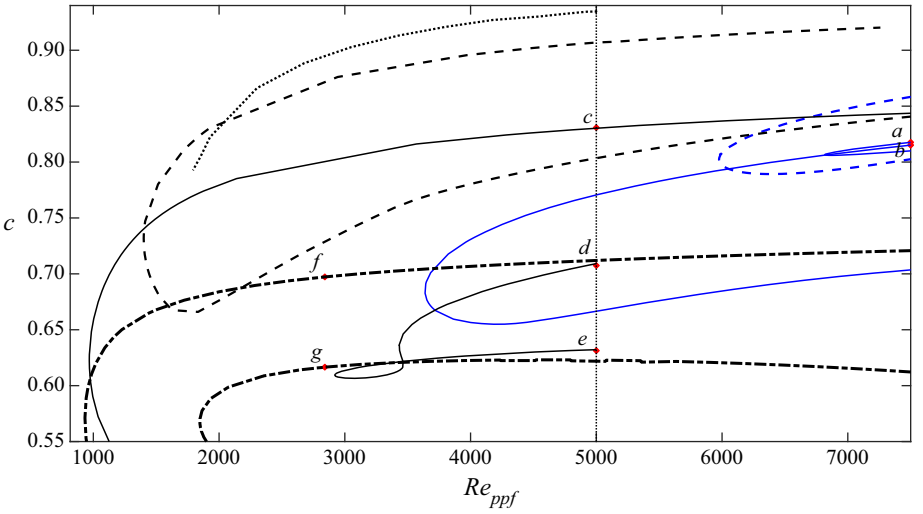


Figure 7. The Re_{ppf} versus c for elliptical pipes at various aspect ratios A for $k_0 = 1$ (black) and $k_0 = 2$ (blue): $A = 1.76$ (solid), $A = 1/1.76$ (dash-dotted), $A = 3.36$ (dashed) and $A = 9.38$ (dotted). When $k_0 = 2$, $\alpha_{ppf} = 1.55$; when $k_0 = 1$, $\alpha_{ppf} = 1.437$ for $A > 1$ and $\alpha_{ppf} = 0.816$ for $A < 1$. The labels a–g correspond to the points a–g in figure 2.

from the saddle-node bifurcation point are identified as the 'upper' and 'lower' branches depending on whether they have lower or higher drag, similarly to their counterparts for circular pipes. Results suggest that TWs without any discrete rotational symmetry exist at much lower Reynolds numbers. From left to right, the first TW solution, which is a rotationally asymmetric TW with $A = 1/1.76$, appears to first exist at the saddle node point $Re_{ppf} = 933$. This solution has top–bottom mirror symmetry after a $\pi/2$-radian rotation around the origin. Next, another rotationally asymmetric solution with left–right mirror symmetry is born out of a saddle node bifurcation at $Re_{ppf} = 968$ with $A = 1.76$. As Re_{ppf} increases, other asymmetric solution branches appear at different aspect ratios. Because of the computational costs, only the lower branch is computed for $A = 9.382$; therefore, the saddle-node point for that branch is not known. For rotationally symmetric solutions, there are two solution branches for $A = 1.76$, with saddle-node points at $Re_{ppf} = 3638$ and $Re_{ppf} = 6817$, and one solution branch for $A = 3.36$, originating at $Re_{ppf} = 5981$.

4. Conclusion

In this paper, we report on numerical computations of TW solutions with shift-and-reflect symmetry through a numerical continuation process using the aspect ratio. We present two new families of solutions found using homotopy continuation starting with circular pipe flow as seen in figure 2. We show that, for the rotationally symmetric case, circular VWI states are not sustained at high aspect ratios; instead, these TWs collapse into modes centred around the middle of the ellipse and connect to a centre-mode TW (figure 4*a*,*b*). On the other hand, the continuation of asymmetric TW simulations reveals a more complex dynamic. A mirror-symmetric (about the y-axis) state has been found to exist (figure 5*a*,*b*) via a direct continuation procedure in elliptical pipes at higher aspect ratios. Further analysis of the asymmetric solutions gives rise to a new solution which has top–bottom symmetry.

https://doi.org/10.1017/jfm.2021.597 Published online by Cambridge University Press

Preliminary calculations suggest that some of these TWs exist at aspect ratios higher than $A = 10.4$, and it is likely that these TW solutions can be continued to much larger aspect ratios. It is worth noting that the rotationally asymmetric VWI states shown in figure 6 resemble the spanwise-localized mirror-symmetric TW1-1 solutions of Gibson, Halcrow & Cvitanovic (2009) in plane Poiseuille flow, which suggests a potential connection between these two solutions. On the other hand, the centre-mode and left–right mirror-symmetric solutions discussed in this paper show characteristics that are very different from those of existing TWs in plane Poiseuille flow. The waves of centre modes are localized around the core as seen in figure 4, unlike the core modes discussed in Park & Graham (2015), where there is a distinct separation of positive and negative waves in the core. It is likely that these new elliptical TWs may be connected to as yet unknown spanwise localized core modes in plane Poiseuille flow.

Supplementary material. Supplementary material is available at https://doi.org/10.1017/jfm.2021.597.

Funding. This work was supported by the Australian Research Council (ARC DP 170104703).

Declaration of interests. The authors report no conflict of interest.

Author ORCIDs.
Ozge Ozcakir https://orcid.org/0000-0002-8672-344X;
Philip Hall https://orcid.org/0000-0001-5175-3115.

References

Davey, A. & Salwen, H. 1994 On the stability of flow in an elliptic pipe which is nearly circular. *J. Fluid Mech.* **281**, 357–369.

Deguchi, K. & Hall, P. 2014 Canonical exact coherent structures embedded in high Reynolds number flows. *Phil. Trans. R. Soc.* A **372** (2020), 20130352.

Deguchi, K. & Walton, A.G. 2013 A swirling spiral wave solution in pipe flow. *J. Fluid Mech.* **737**, R2.

Faisst, H. & Eckhardt, B. 2003 Traveling waves in pipe flow. *Phys. Rev. Lett.* **91**, 224502.

Gibson, J. & Brand, E. 2014 Spanwise-localized solutions of planar shear flows. *J. Fluid Mech.* **745**, 25–61.

Gibson, J.F., Halcrow, J. & Cvitanovic, P. 2009 Equilibrium and travelling-wave solutions of plane Couette flow. *J. Fluid Mech.* **638**, 243–266.

Hall, P. & Sherwin, S. 2010 Streamwise vortices in shear flows: harbingers of transition and the skeleton of coherent structures. *J. Fluid Mech.* **661**, 178–205.

Hall, P. & Smith, F. 1991 On strongly nonlinear vortex/wave interactions in boundary layer transition. *J. Fluid Mech.* **227**, 641–666.

Hocking, L.M. 1977 The stability of flow in an elliptic pipe with large aspect ratio. *Q. J. Mech. Appl. Maths* **30**, 343–353.

Hof, B., van Doorne, C., Westerweel, J., Nieuwstadt, F., Faisst, H., Eckhardt, B., Wedin, H., Kerswell, R. & Waleffe, F. 2004 Experimental observation of nonlinear traveling waves in the turbulent pipe flow. *Science* **305** (5690), 1594–1598.

Kerswell, R.R. & Davey, A. 1996 On the linear instability of elliptic pipe flow. *J. Fluid Mech.* **316**, 307–324.

Nagata, M. & Deguchi, K. 2013 Mirror-symmetric exact coherent states in plane Poiseuille flow. *J. Fluid Mech.* **735**, R4.

Okino, S. 2011 Nonlinear traveling wave solutions in a square duct flow. PhD thesis, Kyoto University.

Ozcakir, O., Hall, P. & Tanveer, S. 2019 Nonlinear exact coherent structures in pipe flow and their instabilities. *J. Fluid Mech.* **868**, 341–368.

Ozcakir, O., Tanveer, S., Hall, P. & Overman, E.A. 2016 Travelling waves in pipe flow. *J. Fluid Mech.* **791**, 284–328.

Park, J. & Graham, M. 2015 Exact coherent states and connections to turbulent dynamics in minimal channel flow. *J. Fluid Mech.* **782**, 430–454.

Pringle, C.C.T. & Kerswell, R.R. 2007 Asymmetric, helical and mirror-symmetric travelling waves in pipe flow. *Phys. Rev. Lett.* **99**, 074502.

https://doi.org/10.1017/jfm.2021.597 Published online by Cambridge University Press

SMITH, F.T. 1979 Instability of flow through pipes of general cross-section, part 1. *Mathematika* **26** (2), 187–210.

SMITH, F.T. & BODONYI, R.J. 1982 Amplitude-dependent neutral modes in the Hagen–Poiseuille flow through a circular pipe. *Proc. R. Soc. Lond.* A **384**, 463–489.

VISWANATH, D. 2009 Critical layer in pipe flow at high Reynolds number. *Phi. Trans. R. Soc.* A **580**, 561–576.

WALEFFE, F. 2001 Exact coherent structures in channel flow. *J. Fluid Mech.* **435**, 93–102.

WALEFFE, F. 2003 Homotopy of exact coherent structures in plane shear flows. *Phys. Fluids* **15** (6), 1517–1534.

WEDIN, H., BOTTARO, A. & NAGATA, M. 2009 Three-dimensional traveling waves in a square duct. *Phys. Rev.* E **79** (6 Pt 2), 065305.

WEDIN, H. & KERSWELL, R. 2004 Exact coherent structures in pipe flow: travelling wave solutions. *J. Fluid Mech.* **508**, 333–371.

https://doi.org/10.1017/jfm.2021.597 Published online by Cambridge University Press